


Efficient steady-state-entanglement generation in strongly driven coupled qubitsAna Laura Gramajo ^{1,2}, Daniel Domínguez,¹ and María José Sánchez ^{1,3}¹*Centro Atómico Bariloche and Instituto Balseiro (Universidad Nacional de Cuyo), 8400 San Carlos de Bariloche, Argentina*²*The Abdus Salam International Center for Theoretical Physics, Strada Costiera 11, 34151 Trieste, Italy*³*Instituto de Nanociencia y Nanotecnología (INN), CONICET-CNEA, 8400, Argentina*

(Received 30 June 2021; accepted 27 August 2021; published 10 September 2021)

We report on a mechanism to optimize the generation of steady-state entanglement in a system of coupled qubits driven by microwave fields. Due to the interplay between Landau-Zener-Stückelberg-Majorana pumping involving three levels and a subsequent fast relaxation channel, which is activated by tuning the qubits-reservoir couplings, a maximally entangled state can be populated. This mechanism does not require the fine tuning of multiphoton resonances but depends on the sign of the qubit-qubit coupling. In particular, we find that by a proper design of the system parameters and the driving protocol, the two-qubit steady-state concurrence can attain values close to 1 in a wide range of driving amplitudes. Our results may be useful to gain further insight into entanglement control and manipulation in dissipative quantum systems exposed to strong driving.

DOI: [10.1103/PhysRevA.104.032410](https://doi.org/10.1103/PhysRevA.104.032410)**I. INTRODUCTION**

The creation of on-demand entangled states for coupled qubit systems exposed to dissipative environments is a challenging requirement to be fulfilled for most quantum operations. It is thus crucial to study the generation and control of entanglement in open quantum systems. Several proposals have shown that noise and coupling to the environment can be used in certain situations to obtain steady-state entanglement from dissipative processes. Besides the specific design of the qubit-qubit interaction, strategies based on engineering the quantum reservoir or the system-reservoir coupling in order to stabilize entanglement and to achieve quantum controlled state preparation have been tested [1–11]. These approaches require an external coherent driving field, and following this route two different regimes have been explored so far.

For weak resonant driving, experimental demonstrations of entanglement stabilization are based on tailoring the relaxation rates in order to generate a nontrivial nonequilibrium dynamics which leads to a highly entangled steady state. Examples of these strategies have been followed in atomic ensembles [4], trapped ions [3,5,9], and superconducting qubits [7,8,10,12,13] and in a general basis involve three levels and the tuning of specific resonances among them. More recently, Ref. [14] proposed a frequency modulation of a periodically pumped laser to achieve an accelerated formation of dissipative entangled steady state in Rydberg atoms.

For nonresonant and *large*-amplitude periodic drivings, a mechanism relying on the amplitude modulation of the periodic (ac) signal was recently proposed for generating dissipative steady-state entanglement in a solid-state qubits system interacting with a thermal bath [15]. In analogy to well-known protocols used to study Landau-Zener-Stückelberg-Majorana (LZSM) interferometry, multiphoton resonances [16–25], and

bath-mediated population inversion [26–29] in two-level systems, entanglement in the steady state has been induced and tuned by changing the amplitude of the ac field in a system composed of two driven and coupled superconducting qubits.

Interestingly, and depending on the relevant time scales, three different scenarios for entanglement evolution have been found in Ref. [15]: (i) a dynamic generation of entanglement at multiphoton resonances for time scales below the decoherence time, in accordance with previous results for nondissipative evolutions [30–32], (ii) *entanglement blackout*, or entanglement destruction due to decoherence with the environment, for times scales longer than decoherence but shorter than the relaxation time, and (iii) the generation of steady-state entanglement out of but close to specific multiphoton resonances for long times (above the relaxation time), with the possibility to enhance entanglement by tuning the driving amplitude. As has been discussed in detail in Ref. [15], the generation of steady-state entanglement requires two levels and some fine tuning of parameters in order to be close to but out of specific resonances, a fact that could be considered as a possible limitation for the proposed scheme.

The high tunability of superconducting qubits, besides demonstrating the full control of the inductive, capacitive, and Ising-like type of coupling between qubits [33–36], enables to efficiently modify the coupling strengths between each qubit and the electromagnetic environment [37–42]. As we show in this work this last tool opens a new avenue for steady-state-entanglement stabilization. By considering that each qubit is coupled with a different strength to the thermal bath, it may be possible to create steady-state maximal entanglement in an efficient way without fine tuning of a particular multiphoton resonance. In this case, the entanglement creation involves three levels and the relaxation is dominated by a decay channel whose contribution is negligible in the case of identical qubit-bath couplings strengths.

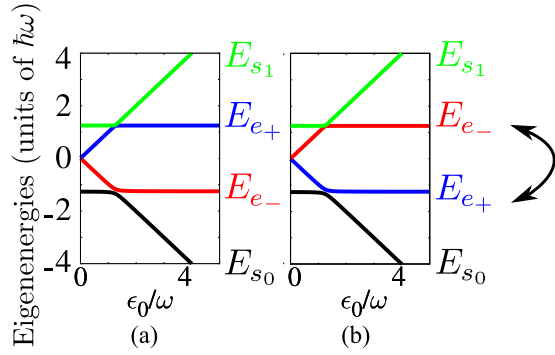


FIG. 1. Eigenenergies of H_0 as a function of ϵ_0/ω for $J/\omega = -2.5$ (a) and $J/\omega = 2.5$ (b). Both spectra are computed for $\Delta_2/\Delta_1 = 1.5$, and $\Delta_1/\omega = 0.1$. For further analysis we normalized parameters in terms of ω . See text for details.

The paper is organized as follows: in Sec. II we introduce the physical model and the Hamiltonian for two coupled qubits driven by strong ac fields. In addition we define the system-bath configuration employed to compute the dissipative open-system dynamics. In Sec. III we analyze the off-resonance three-level (O3L) mechanism for entanglement creation. Other scenarios which involve the tuning of specific resonance conditions for entanglement generation are discussed in Sec. IV, where we also explain why in these cases the steady-state entanglement is lower than for the O3L. Conclusions and perspectives are given in Sec. V.

II. PHYSICAL MODEL

We consider two coupled qubits with Hamiltonian $H_s(t) = H_0 + V(t)$, where

$$H_0 = \sum_{i=1}^2 \left(-\frac{\epsilon_0}{2} \sigma_z^{(i)} - \frac{\Delta_i}{2} \sigma_x^{(i)} \right) - \frac{J}{2} (\sigma_+^{(1)} \sigma_-^{(2)} + \sigma_-^{(1)} \sigma_+^{(2)})$$

and $\sigma_{x,y,z}^{(i)}$ are the Pauli matrices in the Hilbert space of qubit i . The parameters Δ_1 , Δ_2 , and J are fixed by device design and ϵ_0 can be controlled experimentally. This type of Hamiltonian can be realized, for instance, in superconducting qubits [33,43–48] where the qubit-qubit interaction term gives rise to nontrivial entangled (eigen)states of H_0 . The additional term

$$V(t) = -A \cos(\omega t) (\sigma_z^{(1)} + \sigma_z^{(2)})/2,$$

which contains the external ac field of amplitude A and frequency ω [30–32,49–52], is usually implemented to study LZSM interferometry in driven qubits [16,53].

Figure 1 shows the energy spectra of H_0 as a function of the detuning ϵ_0 for $J < 0$ [Fig. 1(a)] and $J > 0$ [Fig. 1(b)]. In both cases, the Hamiltonian H_0 for $\Delta_1, \Delta_2 \ll \epsilon_0$ has two entangled eigenstates $|e_{\pm}\rangle \approx \frac{1}{\sqrt{2}}(|01\rangle \pm |10\rangle)$ (in the basis spanned by the eigenstates of $\sigma_z^{(1)} \otimes \sigma_z^{(2)}$) with eigenenergies $E_{e_{\pm}} \approx \mp |J|/2$, and two separable eigenstates $|s_0\rangle \approx |00\rangle$ and $|s_1\rangle \approx |11\rangle$, with eigenenergies $E_{s_0} \approx -\epsilon_0$ and $E_{s_1} \approx \epsilon_0$, respectively.

In the following we label the states by $|k\rangle$, with $k = 0, \dots, 3$, according to their energy ordering. For instance, the

ground state is $|0\rangle$, the first excited state is $|1\rangle$, and so on. The energy ordering of the separable and entangled states depends on the sign of J and on the value of ϵ_0 relative to $\epsilon_c = |J|/2$, as can be seen in Fig. 1. Notice that the ground state is entangled ($|0\rangle \approx |e_{\mp}\rangle$) for $|\epsilon_0| < \epsilon_c$ and separable ($|0\rangle \approx |s_0\rangle$) for $|\epsilon_0| > \epsilon_c$.

To analyze the open system dynamics it is customary to model the thermal environment by a harmonic-oscillator bath described by a Hamiltonian H_b and the coupling between the system and the bath, H_{sb} , where the global Hamiltonian $\mathcal{H}(t) = H_s(t) + H_b + H_{sb}$. We choose $H_{sb} = \mathcal{A} \otimes \mathcal{B}$, where \mathcal{B} is an observable of the bath and

$$\mathcal{A} = \gamma_1 \sigma_z^{(1)} + \gamma_2 \sigma_z^{(2)}, \quad (1)$$

the system operator which, under the assumption of weak system-bath interaction, is taken linear in the coupling strengths $\gamma_{1,2}$. Notice that other functional forms for the \mathcal{A} operator can be also considered, but we use this one in order to model a realistic situation for superconducting qubits coupled to the electromagnetic environment, that we consider as a thermal bath at temperature T_b and with an Ohmic spectral density $J(\Omega) = \kappa \Omega e^{-|\Omega|/\omega_c}$.

The dynamics of the reduced density matrix of the two coupled qubits $\rho(t) = \text{Tr}_b(\rho_{\text{tot}})$ is obtained by tracing out the degrees of freedom of the bath from the global density matrix ρ_{tot} . We numerically solve the corresponding quantum master equation for the reduced density matrix, under the Floquet-Born-Markov approach [15,29,54–56], which allows the treatment of open systems under periodic drivings of arbitrary strength and frequency (more details are given in Appendix A). The entanglement between the two qubits is quantified by the concurrence, which is defined as $C = \max\{0, \lambda_4 - \lambda_3 - \lambda_2 - \lambda_1\}$, where λ_i 's are the real eigenvalues in decreasing order of the matrix $R = \sqrt{\sqrt{\rho} \tilde{\rho} \sqrt{\rho}}$, with $\tilde{\rho} = \sigma_y^{(1)} \otimes \sigma_y^{(2)} \rho^* \sigma_y^{(1)} \otimes \sigma_y^{(2)}$ [57]. From $\rho(t)$ and $\bar{\rho}_{\infty}$ (where the overline means averaged over one driving period $2\pi/\omega$) we compute the time-dependent and the steady-state concurrences, $C(t)$ and C_{∞} , respectively, when the system is initially prepared in a separable (ground) state of H_0 .

III. STEADY-STATE-ENTANGLEMENT GENERATION: OFF-RESONANCE THREE-LEVEL MECHANISM

In a previous work [15] we have shown that for a strong ac driving, i.e., for large enough amplitudes A , steady-state entanglement can be generated near some multiphoton resonances, when the initial ground state is disentangled (a condition that in our model corresponds to $|\epsilon_0| > \epsilon_c$).

The entanglement generation studied in Ref. [15] assumed that both driven qubits were coupled to the thermal bath with the same strength [$\gamma_1 = \gamma_2$ in Eq.(1)].

In the following, we extend the analysis by considering $\gamma_2 = \xi \gamma_1$, where $\xi \leq 1$ is the parameter that quantifies the relative degree of coupling between each qubit and the thermal bath. As we will show, for $\xi \neq 1$ and $\Delta_1 \neq \Delta_2$ an extra relaxation channel opens, providing a new avenue to maximize the steady-state concurrence and enlarge significantly the region in parameter space where entanglement can be generated.

Hereafter we fix $\Delta_2/\Delta_1 = 1.5$, $\Delta_1 = 0.1\omega$, the bath temperature $T_b/\omega = 0.00467$ (~ 20 mK for typical

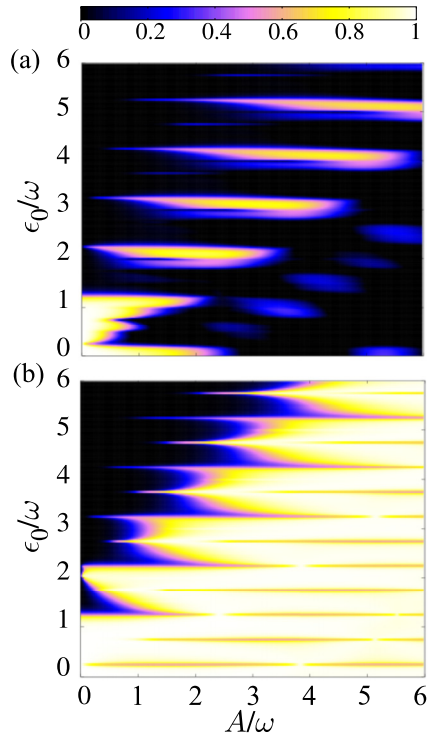


FIG. 2. Color map of C_∞ versus A/ω and ϵ_0/ω for (a) $\xi = 1$ and (b) $\xi = 0.1$, with $\gamma_1 = \gamma$ and $\gamma_2 = \xi\gamma_1$. Both cases are computed for $J/\omega = -2.5$. See text for details.

superconducting qubits), and $\kappa = 0.001$. We also set $\gamma_1 = 1$ and $\gamma_2 = \xi$ for numerical calculations.

We will analyze in what follows the results for $J < 0$. Figure 2 shows the intensity plot of the steady-state concurrence C_∞ as a function of A/ω and ϵ_0/ω for $J/\omega = -2.5$. For this case, we have chosen two different couplings in the system operator \mathcal{A} [Eq. (1)]: $\xi = 1$ [Fig. 2(a)], already studied in Ref. [15], and $\xi = 0.1$ [Fig. 2(b)], corresponding to very dissimilar qubit-bath couplings. As it is evident, the steady-state concurrence exhibits striking differences.

For $\xi = 1$, the structure of C_∞ shown in Fig. 2(a) has been explained in Ref. [15]. There is entanglement generation for $|\epsilon_0| > \epsilon_c$ as a result of a near-resonance mechanism involving two levels (N2L) [28,29], mediated by the interplay of the external driving and the relaxation process that induce the required population inversion. In particular, the N2L mechanism takes place for $\epsilon_0 > \epsilon_c$ near (but out of) a specific multiphoton resonance condition, that sets the energy difference between the separable ground state $|0\rangle \approx |s_0\rangle$ and the entangled state $|e_-\rangle$ to $\Delta E_{se} \sim \epsilon_0 - |J|/2 = n\omega$ with $n \in \mathbb{Z}$ [15]. For these cases, and by adequately tuning a range of driving amplitudes A , the system can be excited from the initial ground state to a virtual multiphoton state, which in the steady state relaxes to the maximally entangled Bell's state $|e_-\rangle$ (notice that this implies having attained population inversion). Thus a steady concurrence $C_\infty \lesssim 1$ is obtained near these resonances by tuning the amplitude A , as it is displayed in Fig. 2(a).

For $\xi = 0.1$ the steady-state concurrence exhibits a very different behavior: $C_\infty \simeq 1$ in Fig. 2(b) over almost all the available parameter space $\{A, \epsilon_0\}$, without requiring a specific

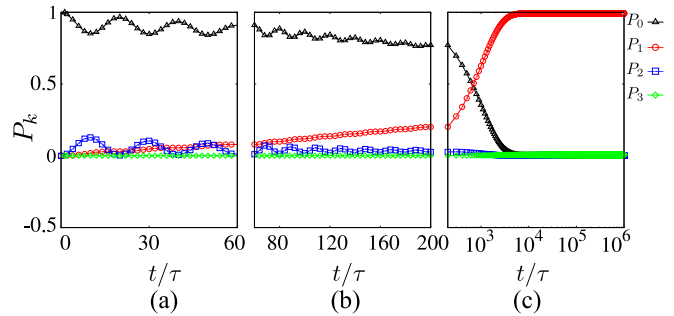


FIG. 3. Plots of the populations P_k , computed in the eigenstates basis of H_0 , as a function of normalized time t/τ ($\tau = 2\pi/\omega$) for $\xi = 0.1$. Plots (a) and (b) are in linear time scale, while plot (c) is in logarithmic scale. The detuning is $\epsilon_0/\omega = 3.7$ (off resonance) and the driving amplitude $A/\omega = 3.8$. Other parameters are the same as in Fig. 2.

“close to a resonance” condition. Notice that the region $|\epsilon_0| < \epsilon_c$ is entangled for amplitudes $A \rightarrow 0$, as the initial ground state is entangled for detunings satisfying the above condition.

As we will discuss below, this new behavior results from an O3L mechanism based on (i) Landau-Zener pumping from the ground state $|0\rangle$ to an ancillary excited state $|2\rangle$ and (ii) fast relaxation from the ancillary $|2\rangle$ to the entangled state $|1\rangle \approx |e_-\rangle$. The sequence of transitions $|0\rangle \rightarrow |2\rangle \rightarrow |1\rangle$ leads to a continuous transfer of population from the ground state $|0\rangle \approx |s_0\rangle$ to the entangled state $|1\rangle \approx |e_-\rangle$, thus giving a steady state with concurrence $C_\infty \simeq 1$.

To illustrate the O3L mechanism $|0\rangle \rightarrow |2\rangle \rightarrow |1\rangle$, we start by computing for $\xi = 0.1$ the diagonal elements (populations) of the two-qubit reduced density matrix $\rho_{kk}(t)$ ($k = 0, \dots, 3$) as a function of time t , in a typical off-resonance case $\epsilon_0/\omega = 3.7$, and for a driving amplitude $A/\omega = 3.8$.

As it is shown in Fig. 3(a), the short-time dynamics induced by the driving mainly involves the coherent evolution of two states: the initial ground state $|0\rangle$ and the second excited state $|2\rangle$, to which population is transferred via the driving-induced Landau-Zener transitions at the energy level avoided crossing (*Landau-Zener pumping*). A necessary condition to accomplish this is that the driving amplitude A must be enough to reach the avoided crossing at $\epsilon_0 = \epsilon_c$, i.e., $A > A_c \equiv |\epsilon_0| - \epsilon_c$. Therefore, $A \sim A_c$ is the characteristic crossover amplitude necessary to activate the Landau-Zener pumping here described ($|0\rangle \rightarrow |2\rangle$ transfer).

For the present case of Fig. 3(a) is $A = 3.8\omega > A_c = 2.45\omega$ and thus Landau-Zener pumping is active. Notice that since $\epsilon_0/\omega = 3.7$ does not correspond to a resonance among these two states, there is only a partial transfer of population from $|0\rangle \rightarrow |2\rangle$.

As time increases [Fig. 3(b)], a direct transition from the ancillary state $|2\rangle$ to the state $|1\rangle$ takes place. The population $\rho_{11}(t)$ of the first excited state starts to grow while the decay of the $\rho_{22}(t)$ and $\rho_{00}(t)$ populations is evident. Finally, for long times after full relaxation, the entangled first excited state $|1\rangle \approx |e_-\rangle$ is fully populated [see Fig. 3(c)]. This *fast relaxation* transition is possible whenever the relaxation mechanism is dominated by the decay rate Γ_{12} connecting the states $|2\rangle \rightarrow |1\rangle$, as we will analyze below.

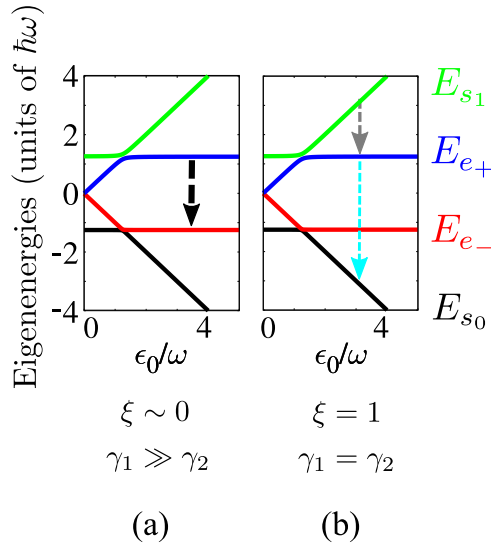


FIG. 4. Eigenenergy spectrum as a function of ϵ_0/ω . The most relevant relaxation processes for (a) $\xi \sim 0$ and (b) $\xi = 1$ are sketched by arrows. The results correspond to $J/\omega = -2.5$, $\epsilon_0 = 3.7\omega$, and no driving, i.e., $A/\omega = 0$. Other parameters are the same as in Fig. 2.

A first and straightforward estimate of the transition rates between the eigenstates $|l\rangle$ and $|k\rangle$ can be obtained from a Fermi golden rule (FGR) calculation

$$\Gamma_{kl} = \frac{2\pi}{\hbar} g(E_{lk}) |\langle l|A|k\rangle|^2, \quad (2)$$

where A is the observable of the system defined in Eq. (1), $E_{lk} = E_l - E_k$, and $g(E)$ accounts for the bath spectral density and thermal factors (see Appendix C). Since we are considering low temperatures, thermal excitations are negligible and thus the relevant decay rates are Γ_{kl} for $l > k$. A perturbative calculation for $\Delta_1, \Delta_2 \ll |\epsilon_0|$ gives for $\epsilon_0 > \epsilon_c$ (see Appendix C for the complete derivation)

$$\begin{aligned} \Gamma_{12} &\propto (1 - \xi)^2, \\ \Gamma_{02} &\propto \left(\frac{\bar{\Delta}}{\epsilon_c}\right)^2 (1 + \xi)^2, \\ \Gamma_{23} &\propto \left(\frac{\bar{\Delta}}{\epsilon_c}\right)^2 (1 + \xi)^2, \\ \Gamma_{01} &\propto \left(\frac{\bar{\Delta}}{\epsilon_c}\right)^2 (1 - \xi)^2, \end{aligned} \quad (3)$$

with $\bar{\Delta} = (\Delta_1 + \Delta_2)/2$, neglecting terms depending on $|\Delta_1 - \Delta_2| < \bar{\Delta}$, and prefactors (of the order of unity) depending on ϵ_0/ϵ_c .

From Eq. (3) it is clear that for $\xi = 1$, Γ_{12} vanishes and the largest transition rates are Γ_{23} and Γ_{02} . In this case the system will tend to relax to the ground state $|s_0\rangle$, as Fig. 4(b) shows schematically. On the other hand, for $\xi \rightarrow 0$ the rate Γ_{12} attains its maximum value and is by far the largest one, providing the fast relaxation mechanism that results in the entangled state $|e_-\rangle$ being fully populated, also shown schematically in Fig. 4(a). We plot in Fig. 5(a) the most relevant relaxation rates as a function of ξ , estimated with the FGR and using the

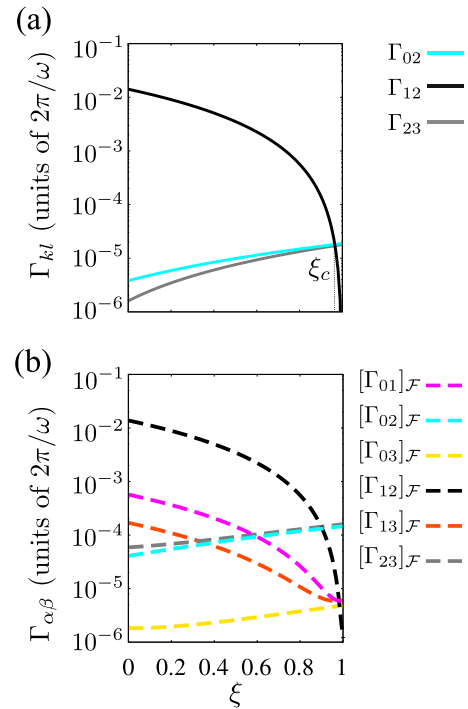


FIG. 5. Plots of the transition rates as a function of ξ for the off-resonance case $\epsilon_0 = 3.7\omega$. (a) Analytical results Γ_{kl} computed in the eigenstate basis, employing Eq. (C2) of Appendix C. The value of ξ_c is indicated. (b) $\Gamma_{\alpha\beta}$ computed in the Floquet basis for $A/\omega = 3.8\omega$. Other parameters are the same as in Fig. 2.

full expressions given in Appendix C. As can be seen, there is a characteristic $\xi = \xi_c$ such that $\Gamma_{02}, \Gamma_{23} \gg \Gamma_{12}$ for $\xi > \xi_c$ and $\Gamma_{12} \gg \Gamma_{02}, \Gamma_{23}$, for $\xi < \xi_c$. From Eq. (3), one obtains $1 - \xi_c \propto \bar{\Delta}/\epsilon_c$.

To simplify the analytical calculations, we have neglected the dependence of Γ_{kl} on the driving amplitude, since we have computed the transition rates among eigenstates of the undriven Hamiltonian H_0 . However, the natural basis to compute the transition rates in the case of a strongly driven system is the Floquet basis \mathcal{F} , in which the density matrix in the steady state becomes diagonal [29]. Following this route, in Fig. 5(b) we plot the transition (relaxation) rates $\Gamma_{\alpha\beta}$ computed numerically in the Floquet basis \mathcal{F} [15,28,29] as a function of ξ , for the considered off-resonant situation, $\epsilon_0/\omega = 3.7$.

To each Floquet state we can associate the H_0 eigenstate to which it tends for $A \rightarrow 0$. We have then labeled the Floquet states $\alpha, \beta, \gamma, \delta$ following the same ordering as the eigenstates of H_0 (this is a reasonable choice since quasienergies do not cross for out-of-resonance conditions [21,28,58]). Notice that the rates in the Floquet basis, $[\Gamma_{12}]_{\mathcal{F}}$, $[\Gamma_{02}]_{\mathcal{F}}$, and $[\Gamma_{23}]_{\mathcal{F}}$, have a functional dependence on ξ similar to the estimates given in Eq. (3), and shown in Fig. 5(a). In particular for $\xi = 1$ the largest transition rates are $[\Gamma_{23}]_{\mathcal{F}}$ and $[\Gamma_{02}]_{\mathcal{F}}$, while for $\xi \rightarrow 0$ the relaxation process is dominated by $[\Gamma_{12}]_{\mathcal{F}}$, in correspondence with the previous description. As it is discussed in Appendix C, for out-of-resonance situations the rates computed in the Floquet basis, $\Gamma_{\alpha\beta}$, give essentially the same qualitative information regarding the main relaxation processes as the rates computed in the eigenbasis of H_0 , Γ_{kl} .

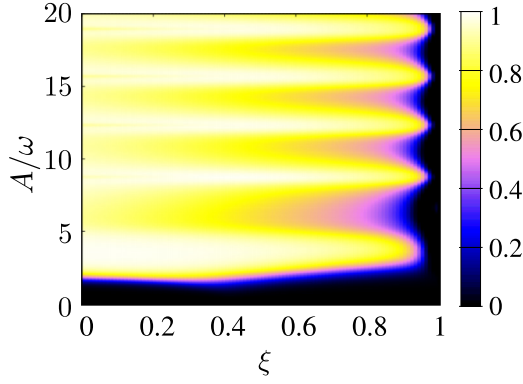


FIG. 6. Intensity plot of C_∞ versus ξ and A/ω for the off-resonance case $\epsilon_0/\omega = 3.7$. Other parameters are the same as in Fig. 2.

Taking into account that the most accurate description is in terms of the Floquet transition rates, the crossover ξ_c should be defined from the condition $[\Gamma_{12}]_{\mathcal{F}} = [\Gamma_{02}]_{\mathcal{F}}$. Thus in general ξ_c will depend on the driving amplitude A .

From the above discussion we stress that to attain the O3L mechanism the conditions $A \gtrsim A_c$ (Landau-Zener pumping) and $\xi \lesssim \xi_c$ (fast relaxation) have to be fulfilled simultaneously. This is confirmed in Fig. 6, where C_∞ is plotted as a function of ξ and A/ω for the mentioned off-resonance condition. For $\xi = 1$ there is no noticeable entanglement creation for all the explored values of the amplitude A [see also Fig. 2(a) for $\epsilon_0/\omega = 3.7$], while for $\xi < \xi_c$, a finite concurrence $C_\infty > 0$ is obtained. It is also clear from Fig. 6 that ξ_c has a modulation with A , as expected from the previous discussion on the Floquet relaxation rates.

We emphasize that driving and dissipation are the two key ingredients to generate entanglement, as in the case of identical qubit-bath couplings studied in Ref. [15]. However, the entanglement generation here described does not require to tune a given resonance condition but to tailor the system-bath interaction to allow for the needed relaxation channel.

So far we have shown that the generation of steady-state entanglement for $\xi \neq 1$ and for off-resonant situations relies on the O3L mechanism described along this section. Despite that we have focused on a specific value of $J = -2.5\omega$, the O3L mechanism rules the generation of entanglement in off-resonant situations for $\xi \neq 1$ and general values of $J < 0$, as we discuss in Appendix D.

However, the O3L mechanism is completely suppressed for $J > 0$. In this case the first and second excited states are switched between each other, $|e_-\rangle \leftrightarrow |e_+\rangle$ ($1 \leftrightarrow 2$). In particular for $\xi \rightarrow 0$, in addition to $[\Gamma_{12}]_{\mathcal{F}}$, the second relevant relaxation rate becomes $[\Gamma_{02}]_{\mathcal{F}}$, activating the decay process $|2\rangle \rightarrow |0\rangle$ that tends to populate the ground state at long times (see Appendix D for a detailed discussion).

IV. DYNAMICS OF ENTANGLEMENT GENERATION AT RESONANCES

The reduction in the amount of entanglement at resonances $\epsilon_0 \pm |J|/2 \sim m\omega$ is evident, for example, in Fig. 2, along the

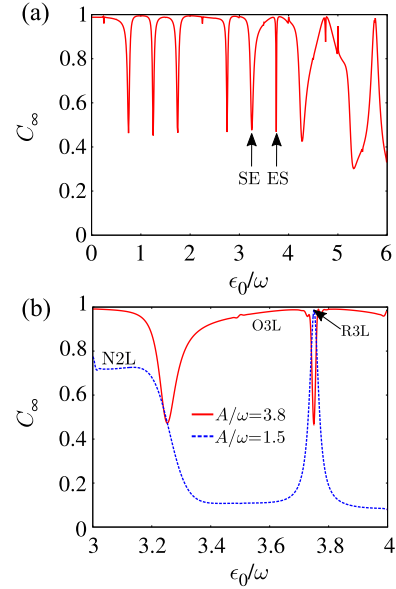


FIG. 7. (a) Plot of C_∞ as a function of ϵ_0/ω for the driving amplitude $A/\omega = 3.8$. The resonances $\epsilon_0/\omega = 3.25$ (SE) and $\epsilon_0/\omega = 3.75$ (ES) are indicated by arrows. (b) Zoom-in plot near the SE and ES resonances for amplitudes $A/\omega = 3.8$ (red) and $A/\omega = 1.5$ (blue). The labels N2L, R3L, and O3L indicate the main mechanisms for entanglement generation described in the text. Other parameters are the same as in Fig. 2.

straight lines where $C_\infty \sim 0.5$, and in Fig. 7(a), where we plot C_∞ as a function of ϵ_0 for $A = 3.8\omega$.

We distinguish two types of resonances: (i) resonances between the separable state $|0\rangle$ and the entangled state $|1\rangle$, for $\epsilon_0 \sim m\omega + |J|/2$, which we name SE resonance, and (ii) resonances between the entangled state $|1\rangle$ and the separable state $|3\rangle$, for $\epsilon_0 \sim m\omega - |J|/2$, which we name ES resonance. In what follows we will study the detailed dynamics of entanglement generation for two examples of these resonances, $\epsilon_0/\omega = 3.25$ (SE) and $\epsilon_0/\omega = 3.75$ (ES), which are indicated by arrows in Fig. 7(a).

The time evolution of the populations, $P_k(t) = \langle k|\rho(t)|k\rangle$, computed in the eigenstate basis of H_0 is shown in Fig. 8 for $\epsilon_0/\omega = 3.25$, which, as we mentioned, corresponds to a mul-

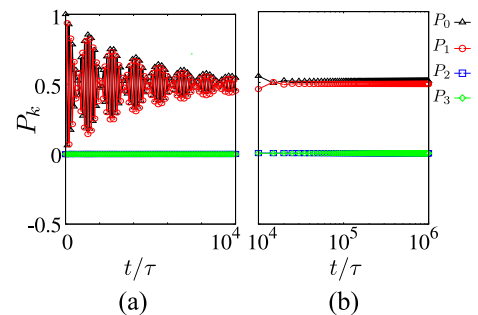


FIG. 8. Plots of the populations P_k , computed in the eigenstates basis of H_0 , as a function of normalized time t/τ ($\tau = 2\pi/\omega$) for $\xi = 0.1$. The detuning is $\epsilon_0/\omega = 3.25$ (SE resonance) and the driving amplitude is $A/\omega = 3.8$. Other parameters are the same as in Fig. 2. Plot (a) is in linear time scale and plot (b) in logarithmic time scale.

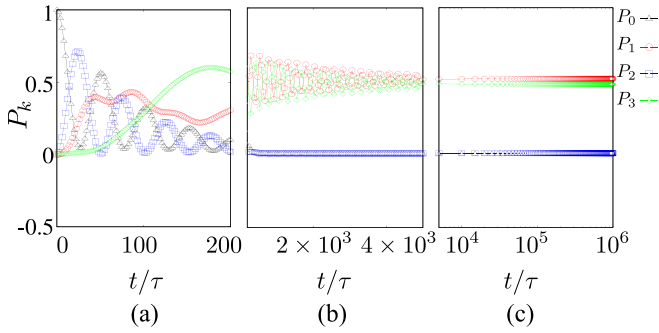


FIG. 9. Plots of the populations P_k computed in the eigenstate basis of H_0 , as a function of normalized time t/τ ($\tau = 2\pi/\omega$) for $\xi = 0.1$. The detuning is $\epsilon_0/\omega = 3.75$ (ES resonance) and the driving amplitude is $A/\omega = 3.8$. Other parameters are the same as in Fig. 2. Plots (a) and (b) are in linear time scale, while plot (c) is in logarithmic scale.

tiphoton resonance condition between the states $\{|0\rangle = |s_0\rangle\}$ and $\{|1\rangle = |e_-\rangle\}$ (SE resonance). Since the initial state is the ground state [$P_0(0) = 1$], at short times there is a coherent oscillatory exchange of population with the first excited state, as shown in Fig. 8(a). Notice that there are not intermediate populated levels ($P_2 = P_3 = 0$), and the coherence between $\{|s_0\rangle, |e_-\rangle\}$ dies off at longer times due to decoherence effects. The final steady-state populations are $P_0 = P_1 = 0.5$ [see Fig. 8(b)]. Since $|0\rangle$ is separable while $|1\rangle$ is an entangled state, a partial entanglement generation is attained with $C_\infty \simeq 0.5$.

The example corresponding to the second type of resonance (ES) is shown for $\epsilon_0/\omega = 3.75$ in Fig. 9, which displays the time evolution of the populations P_k computed in the eigenstate basis. In this case, the dynamics at intermediate times is richer because for this ϵ_0 a simultaneous resonance condition between the states $\{|0\rangle, |2\rangle\}$ and $\{|1\rangle, |3\rangle\}$ takes place. For short times (as the system starts in the ground state) the populations P_0 and P_2 exhibit well-defined Rabi-like oscillations due to the resonance condition. As soon as the $|2\rangle$ state starts to be populated, there is a fast decay from this state to the $|1\rangle$ state, as can be observed for times $t \lesssim 100\tau$ in Fig. 9(a). This $|0\rangle \leftrightarrow |2\rangle \rightarrow |1\rangle$ process corresponds to the standard three-level mechanism at a resonance (R3L), which induces a net transfer of population to the first excited state, mediated by resonant pumping from the ground state to a second excited state. Once the $|1\rangle$ state is populated, the resonance with the $|3\rangle$ dominates the dynamics, giving place to an oscillatory exchange between these two states for times ($t \gtrsim 200\tau$), as shown in Fig. 9(b). These oscillations die off for $t \sim 4.10^3\tau$ due to dissipative effects, and the steady-state system is ultimately reached, as Fig. 9(c) shows. The steady-state populations are $P_1 \sim 0.5$ and $P_3 \sim 0.5$, leading to a concurrence $C_\infty \sim 0.5$.

The difference in the entanglement generation for the two types of resonances becomes more evident for low driving amplitudes. For $A \lesssim A_c$ the O3L mechanism is turned off since the Landau-Zener transfer to higher states is suppressed, and thus the other mechanisms for entanglement generation at resonances are unveiled. This is well illustrated in Fig. 7(b) for the amplitude $A = 1.5\omega < A_c$. Notice that at one side of the

SE resonance ($\epsilon_0/\omega = 3.25$) there is entanglement generation due to the N2L mechanism involving $|0\rangle \leftrightarrow |1\rangle$ and thus the dependence of C_∞ with ϵ_0 is asymmetric around this resonance, as has been already discussed in Ref. [15]. On the other hand, for the ES resonance ($\epsilon_0/\omega = 3.75$), the entanglement generation for low A is through the standard R3L mechanism with resonant pumping $|0\rangle \leftrightarrow |2\rangle$ followed by the fast decay $|2\rangle \rightarrow |1\rangle$. In this case, the dependence of C_∞ with ϵ_0 shows a narrow symmetric peak around this resonance.

V. CONCLUSIONS

We have presented an off-resonance three-level (O3L) mechanism for steady-state entanglement generation in strongly driven qubits. The mechanism does not require the fine tuning of specific photon resonances as in the standard R3L mechanism, and it is not limited to a certain range of driving amplitudes, as in the N2L mechanism [15]. Unlike these cases, the O3L mechanism is efficient to generate steady entanglement in a wide range of parameters, above a threshold of bath coupling asymmetry and driving amplitude.

The proposed strategy for entanglement generation is based on the same principle used for microwave cooling of superconducting qubits in Ref. [59], which essentially consists of the excitation to a higher level through a nonresonant process based on Landau-Zener transitions, plus the tuning of a fast relaxation channel to the desired final state. In the microwave cooling case this protocol has been very efficient to pump population from the first excited state to the ground state, significantly lowering the effective temperature of the qubit. In our case, the O3L mechanism achieves the active pumping of population from the separable ground state to an entangled excited state.

Small gap superconducting qubits are a good architecture to study quantum dynamics and quantum control processes based on Landau-Zener transitions [16,53,59–61]. For instance, Campbell *et al.* [60] have shown recently that through the use of nonresonant Landau-Zener transitions it is possible to achieve high-fidelity single-qubit operations in these devices. Circuits of coupled small-gap superconducting qubits, with added control of the system-bath coupling, are possible candidates for the implementation of the entanglement generation mechanism proposed here.

ACKNOWLEDGMENTS

We acknowledge support from CNEA, CONICET (PIP11220150100756), UNCuyo (P 06/C591), and ANPCyT (PICT2016-0791 and PICT2019/0654).

APPENDIX A: FLOQUET-MARKOV MASTER EQUATION

As mentioned in Sec. II the open system dynamics can be described by the global Hamiltonian $\mathcal{H}(t) = H_s(t) + H_b + H_{sb}$, where $H_s(t) = H_0 + V(t)$ is the Hamiltonian of two coupled qubits H_0 driven by a periodic external field $V(t)$. Since $H_s(t) = H_s(t + \tau)$ is periodic in time, with $\tau = 2\pi/\omega_0$ the driving period, it is customary to employ the Floquet formalism to solve the dynamics [58,62–64]. In the Floquet formalism the solutions of

the time-dependent Schrödinger equation are of the form $|\Psi_\alpha(t)\rangle = e^{i\gamma_\alpha t/\hbar}|u_\alpha(t)\rangle$, where the Floquet states $|u_\alpha(t)\rangle$ satisfy $|u_\alpha(t)\rangle = |u_\alpha(t + \tau)\rangle = \sum_K |u_\alpha(K)\rangle e^{-iK\omega t}$ and are eigenstates of $[\mathcal{H}(t) - i\hbar\partial/\partial t]|u_\alpha(t)\rangle = \gamma_\alpha|u_\alpha(t)\rangle$, with γ_α the associated quasienergy.

We consider a bosonic thermal bath at temperature T_b described by the usual harmonic oscillator Hamiltonian H_b , which is linearly coupled to the two-qubit system in the form $H_{sb} = g\mathcal{A} \otimes \mathcal{B}$, with g the coupling strength, \mathcal{B} an observable of the bath, and \mathcal{A} an observable of the system as defined in Eq. (1). In what follows we consider a bath with an Ohmic spectral density $J(\Omega) = \gamma\Omega e^{-|\Omega|/\omega_c}$, with ω_c the cutoff frequency.

The dynamics of the composed system is ruled by the von Neumann equation

$$\dot{\rho}_{\text{tot}}(t) = -\frac{i}{\hbar}[\mathcal{H}(t), \rho_{\text{tot}}(t)], \quad (\text{A1})$$

which after tracing over the degrees of freedom of the bath becomes an equation for the evolution of the two-qubit reduced density matrix $\rho(t) = \text{Tr}_b(\rho_{\text{tot}}(t))$,

$$\dot{\rho}(t) = -\frac{i}{\hbar}\text{Tr}_b([\mathcal{H}(t), \rho_{\text{tot}}(t)]). \quad (\text{A2})$$

After expanding $\rho(t)$ in terms of the time-periodic Floquet basis $\{|u_\alpha(t)\rangle\}$ ($\alpha, \beta = 0, 1, 2, 3$),

$$\rho_{\alpha\beta}(t) = \langle u_\alpha(t)|\rho(t)|u_\beta(t)\rangle, \quad (\text{A3})$$

the Born (weak-coupling) and Markov (local-in-time) approximations for the time evolution are performed. In this way, the Floquet-Markov master equation [29,54,58,63,65–69] is obtained:

$$\begin{aligned} \dot{\rho}_{\alpha\beta}(t) &= -i(\gamma_\alpha - \gamma_\beta)\rho_{\alpha\beta} - \sum_{\alpha'\beta'} \mathcal{L}_{\alpha\beta,\alpha'\beta'}(t)\rho(t)_{\alpha'\beta'}, \\ \mathcal{L}_{\alpha\beta,\alpha'\beta'}(t) &= \sum_Q \mathcal{L}_{\alpha\beta,\alpha'\beta'}^Q e^{-iQ\omega t}, \end{aligned} \quad (\text{A4})$$

with $\mathcal{L}_{\alpha\beta,\alpha'\beta'}(t)$ the transition rates and $Q \in \mathbb{Z}$. The Fourier coefficients are defined as

$$\begin{aligned} \mathcal{L}_{\alpha\beta,\alpha'\beta'}^Q &= \sum_K (\delta_{\beta\beta'} \sum_\eta g_{\eta\alpha'}^K A_{\alpha\eta}^{K+Q} A_{\eta\alpha}^K \\ &+ \delta_{\alpha\alpha'} \sum_\eta g_{\eta\beta'}^{-K} A_{\eta\beta}^{K+Q} A_{\beta'\eta}^K \\ &- (g_{\alpha\alpha'}^K + g_{\beta\beta'}^{-K-Q}) A_{\alpha\alpha'}^K A_{\beta'\beta}^{K+Q}), \end{aligned} \quad (\text{A5})$$

with $g_{\alpha\beta}^K = J(\gamma_{\alpha\beta} + K\omega)n_{th}(\gamma_{\alpha\beta} + K\omega)$, and $\gamma_{\alpha\beta} = \gamma_\alpha - \gamma_\beta$ and $K \in \mathbb{Z}$. The thermal occupation is given by the Bose-Einstein function $n_{th}(x) = 1/(e^{x/k_B T} - 1)$. Each $A_{\alpha\beta}^K$ is a transition matrix element in the Floquet basis, defined as $A_{\alpha\beta}^K = \sum_L \langle u_\alpha(L)|\mathcal{A}|u_\beta(L+K)\rangle$, with $|u_\alpha(L)\rangle$ the Fourier component of the Floquet state, $L \in \mathbb{Z}$.

By considering that the time scale t_r for full relaxation is $t_r \gg \tau$, the transition rates $\mathcal{L}_{\alpha\beta,\alpha'\beta'}(t)$ can be thus approximated by their average over one period τ , $\mathcal{L}_{\alpha\beta,\alpha'\beta'}(t) \sim$

$\mathcal{L}_{\alpha\beta,\alpha'\beta'}^{Q=0}$ [54,65], obtaining

$$\begin{aligned} \mathcal{L}_{\alpha\beta,\alpha'\beta'}^{Q=0} &= \delta_{\beta\beta'} \sum_\eta R_{\eta\eta,\alpha'\alpha} + \delta_{\alpha\alpha'} \sum_\eta (R_{\eta\eta,\beta'\beta})^* \\ &- R_{\alpha\beta,\alpha'\beta'} - (R_{\beta\alpha,\beta'\alpha'})^*, \end{aligned} \quad (\text{A6})$$

where the rates

$$R_{\alpha\beta,\alpha'\beta'} = \sum_K g_{\alpha\alpha'}^K A_{\alpha\alpha'}^K (A_{\beta\beta'}^K)^* \quad (\text{A7})$$

can be interpreted as sums of K -photon exchange terms.

The numerical procedure is as follows. First, the Floquet components $|u_\alpha(K)\rangle$ are obtained by solving the unitary evolution and, with them, the rates $R_{\alpha\beta,\alpha'\beta'}$ and $\mathcal{L}_{\alpha\beta,\alpha'\beta'}^{Q=0}$ are computed. The time-dependent solution of $\rho_{\alpha\beta}(t)$ and the steady state $\rho_{\alpha\beta}(t \rightarrow \infty)$ are finally calculated as described in Ref. [29].

APPENDIX B: EIGENSTATES OF H_0

In this section, we give analytical expressions for the eigenstates of the undriven system H_0 using perturbation theory in the parameters Δ_i .

We start by writing the Hamiltonian in Eq. (1) as $H_0 = H_0^{(0)} + H_1$, where

$$H_0^{(0)} = \sum_{i=1}^2 -\frac{\epsilon_0}{2}\sigma_z^{(i)} - \frac{J}{2}(\sigma_+^{(1)}\sigma_-^{(2)} + \sigma_-^{(1)}\sigma_+^{(2)}) \quad (\text{B1})$$

and

$$H_1 = \sum_{i=1}^2 -\frac{\Delta_i}{2}\sigma_x^{(i)}. \quad (\text{B2})$$

The eigenstates of $H_0^{(0)}$, spanned in the basis of $\sigma_z^{(1)} \otimes \sigma_z^{(2)}$, can be found by direct diagonalization, with the two Bell states $|e_\pm^{(0)}\rangle = \frac{1}{\sqrt{2}}(|01\rangle \pm |10\rangle)$ with eigenenergies $E_{e_\pm}^{(0)} = \mp|J|/2$ and the two separable eigenstates $|s_0^{(0)}\rangle = |00\rangle$ and $|s_1^{(0)}\rangle = |11\rangle$, with eigenenergies $E_{s_0}^{(0)} = -\epsilon_0$ and $E_{s_1}^{(0)} = \epsilon_0$, respectively. As we have mentioned in the main text, for both signs of J , the ground state of $H_0^{(0)}$ is entangled ($|e_\mp^{(0)}\rangle$) for $|\epsilon_0| < |J|/2$ and separable ($|s_0^{(0)}\rangle$) for $|\epsilon_0| > |J|/2$.

For $\Delta_1, \Delta_2 \ll |\epsilon_0|$, as we assumed in the present analysis, H_1 can be considered as a perturbative term. Straightforward calculations give to first order in perturbation theory

$$\begin{aligned} |s_0\rangle &= |s_0^{(0)}\rangle + \frac{\Delta_-}{\epsilon_0 + J/2}|e_-^{(0)}\rangle + \frac{\Delta_+}{\epsilon_0 - J/2}|e_+^{(0)}\rangle, \\ |s_1\rangle &= |s_1^{(0)}\rangle + \frac{\Delta_-}{\epsilon_0 - J/2}|e_-^{(0)}\rangle - \frac{\Delta_+}{\epsilon_0 + J/2}|e_+^{(0)}\rangle, \\ |e_-\rangle &= |e_-^{(0)}\rangle - \frac{\Delta_-}{\epsilon_0 + J/2}|s_0^{(0)}\rangle - \frac{\Delta_-}{\epsilon_0 - J/2}|s_1^{(0)}\rangle, \\ |e_+\rangle &= |e_+^{(0)}\rangle - \frac{\Delta_+}{\epsilon_0 - J/2}|s_0^{(0)}\rangle + \frac{\Delta_+}{\epsilon_0 + J/2}|s_1^{(0)}\rangle, \end{aligned} \quad (\text{B3})$$

where we define $\Delta_\pm = \frac{\Delta_1 \pm \Delta_2}{2\sqrt{2}}$.

APPENDIX C: TRANSITION RATES

With Eq. (B3) at hand, one can compute the transition rates $\Gamma_{f \leftarrow i} \equiv \Gamma_{fi}$ using the FGR,

$$\Gamma_{fi} = \frac{2\pi}{\hbar} g(E_{if}) |\langle i | \mathcal{A} | f \rangle|^2, \quad (\text{C1})$$

where the indices i and f indicate the initial and final states, respectively, $E_{if} = E_i - E_f$, \mathcal{A} is an observable of the system defined in Eq. (1), and $g(E) = n_{th}(E)J(E/\hbar)$ is written as the product of the Bose-Einstein function n_{th} and $J(\Omega)$, the spectral density of the bath given in Appendix A.

Using Eq. (C1), we obtain

$$\begin{aligned} \Gamma_{12} &\sim \frac{2\pi}{\hbar} g(E_{21}) \gamma_1^2 \left[(1 - \xi) + 2(1 + \xi) \frac{\Delta_- \Delta_+}{(\epsilon_0^2 - \frac{J^2}{4})} \right]^2, \\ \Gamma_{01} &\sim \frac{2\pi}{\hbar} g(E_{10}) \gamma_1^2 \left[(1 - \xi) \frac{\Delta_+}{(\epsilon_0 - \frac{J}{2})} + (1 + \xi) \frac{\Delta_-}{(\epsilon_0 + \frac{J}{2})} \right]^2, \\ \Gamma_{13} &\sim \frac{2\pi}{\hbar} g(E_{31}) \gamma_1^2 \left[(1 - \xi) \frac{\Delta_+}{(\epsilon_0 + \frac{J}{2})} + (1 + \xi) \frac{\Delta_-}{(\epsilon_0 - \frac{J}{2})} \right]^2, \\ \Gamma_{02} &\sim \frac{2\pi}{\hbar} g(E_{20}) \gamma_1^2 \left[(1 + \xi) \frac{\Delta_+}{(\epsilon_0 - \frac{J}{2})} + (1 - \xi) \frac{\Delta_-}{(\epsilon_0 + \frac{J}{2})} \right]^2, \\ \Gamma_{23} &\sim \frac{2\pi}{\hbar} g(E_{32}) \gamma_1^2 \left[(1 + \xi) \frac{\Delta_+}{(\epsilon_0 + \frac{J}{2})} + (1 - \xi) \frac{\Delta_-}{(\epsilon_0 - \frac{J}{2})} \right]^2, \end{aligned} \quad (\text{C2})$$

where the labeling corresponds to the eigenstates ordering given for $J < 0$, while $1 \leftrightarrow 2$ for $J > 0$, as in this case the first and second excited states are $|1\rangle = |e_+\rangle$ and $|2\rangle = |e_-\rangle$, respectively. These expressions correspond to transition rates between the eigenstates of H_0 . Thus, they are adequate for describing the relaxation dynamics in the undriven system or for weak driving amplitudes.

In general, the relaxation dynamics of the strongly driven system should be discussed in terms of the transition rates $\Gamma_{\alpha\beta}$ between Floquet states, which can be obtained as follows. After performing the secular approximation [15], Eq. (A4) transforms into a Lindblad-type equation, given by

$$\dot{\rho} = -i[H_s(t), \rho] + \sum_{\alpha\beta} \Gamma_{\alpha\beta} (L_{\alpha\beta} \rho L_{\alpha\beta}^\dagger - \frac{1}{2} \{L_{\alpha\beta}^\dagger L_{\alpha\beta}, \rho\}), \quad (\text{C3})$$

where $L_{\alpha\beta} = |u_\alpha(t)\rangle\langle u_\beta(t)|$ are the corresponding jump operators, and the transition rates $\Gamma_{\alpha\beta} = R_{\alpha\alpha,\beta\beta}$ can be written as

$$\begin{aligned} \Gamma_{\alpha\beta} &= \sum_n \Gamma_{\alpha\beta}^{(n)}, \\ \Gamma_{\alpha\beta}^{(n)} &= g(\gamma_{\alpha\beta} + n\omega) |A_{\alpha\beta}^n|^2, \end{aligned} \quad (\text{C4})$$

where $\gamma_{\alpha\beta} = \gamma_\alpha - \gamma_\beta$ is the quasienergies difference.

When the driving is weak, for $A \rightarrow 0$, the Floquet states tend to the eigenstates of H_0 , $|u_\alpha(t)\rangle \rightarrow |i\rangle$. Thus, for $A = 0$ the Floquet rates $\Gamma_{\alpha\beta}^{(A=0)}$ coincide with the eigenstate rates Γ_{ij} . In Fig. 10(a) we compare the approximate expressions obtained from Eq. (C2) for the rates Γ_{ij} with the Floquet rates $\Gamma_{\alpha\beta}$ computed numerically for $A = 0$ and $\epsilon_0/\omega = 3.7$. Since

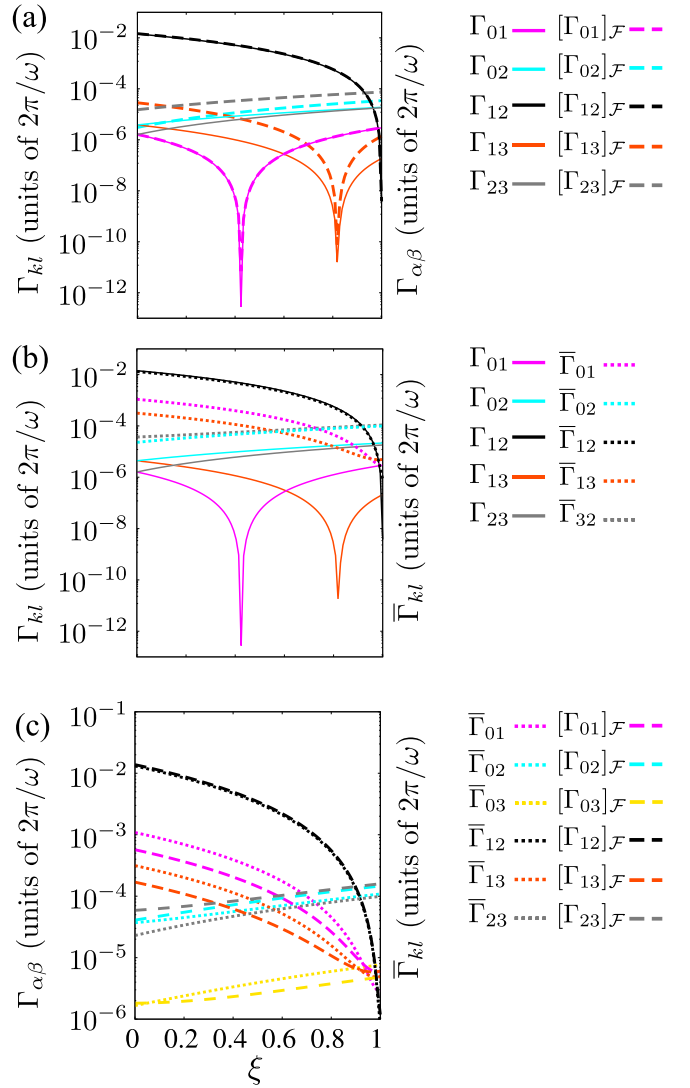


FIG. 10. Plot of the transition rates Γ_{kl} , $\bar{\Gamma}_{kl}$, and $\Gamma_{\alpha\beta}$ as a function of ξ for the off-resonance condition $\epsilon_0/\omega = 3.7$. (a) The rates Γ_{kl} are plotted in the eigenstates basis using the analytical estimates given by Eq. (C2) (bold lines), while $\Gamma_{\alpha\beta}$ are numerically computed in the Floquet basis (dashed lines). Both results correspond to $A/\omega = 0$. (b) Rates Γ_{kl} plotted in (a) and rates $\bar{\Gamma}_{kl}$ computed using Eq. (C9) (dotted lines) for $A/\omega = 3.8$. (c) Rates $\bar{\Gamma}_{kl}$ plotted in (b) and rates $\Gamma_{\alpha\beta}$ computed numerically, both for $A/\omega = 3.8$. Other parameters are the same as in Fig. 2.

$\Delta_1, \Delta_2 \ll |\epsilon_0|$, there is a good agreement between the rates approximated by Eq. (C2) and the exact numerical rates.

In the following we derive effective expressions for the rates Γ_{kl} between the eigenstates for finite driving amplitudes $A \neq 0$ in terms of the Floquet transition rates $\Gamma_{\alpha\beta}$. We start by rewriting Eq. (C3) in the interaction picture, i.e., $\dot{\tilde{\rho}} = U^\dagger(t) \rho U(t)$ with $U(t) = \sum_\alpha e^{-i\gamma_\alpha t} |u_\alpha(t)\rangle\langle u_\alpha(0)|$,

$$\dot{\tilde{\rho}} = \sum_{\alpha\beta} \Gamma_{\alpha\beta} (\tilde{L}_{\alpha\beta} \tilde{\rho} \tilde{L}_{\alpha\beta}^\dagger - \frac{1}{2} \{\tilde{L}_{\alpha\beta}^\dagger \tilde{L}_{\alpha\beta}, \tilde{\rho}\}), \quad (\text{C5})$$

with $\tilde{L}_{\alpha\beta} = |u_\alpha(0)\rangle\langle u_\beta(0)|$.

After performing the basis change (with $H_0|i\rangle = E_i|i\rangle$),

$$\begin{aligned}\tilde{L}_{\alpha\beta} &= \sum_{ij} |i\rangle\langle i|u_\alpha(0)\rangle\langle u_\beta(0)|j\rangle\langle j| \\ &= \sum_{ij} \langle i|u_\alpha(0)\rangle\langle u_\beta(0)|j\rangle L_{ij},\end{aligned}\quad (\text{C6})$$

with $L_{ij} = |i\rangle\langle j|$, and replacing into Eq. (C5), we get

$$\dot{\tilde{\rho}} = \sum_{ijkl} \bar{\Gamma}_{ij,kl} (L_{ij}\tilde{\rho}L_{kl}^\dagger - \frac{1}{2}\{L_{kl}^\dagger L_{ij}, \tilde{\rho}\}), \quad (\text{C7})$$

with

$$\bar{\Gamma}_{ij,kl} = \sum_{\alpha\beta} \langle i|u_\alpha(0)\rangle\langle u_\beta(0)|j\rangle\langle l|u_\beta(0)\rangle\langle u_\alpha(0)|k\rangle\Gamma_{\alpha\beta}. \quad (\text{C8})$$

Further assuming that only diagonal terms dominate when the system is fully relaxed (as each Floquet state has principal weight on the associated eigenstate) the relevant rates in Eq. (C8) are $\bar{\Gamma}_{ij,ij} \equiv \bar{\Gamma}_{ij}$, which read

$$\bar{\Gamma}_{ij} = \sum_{\alpha\beta} |\langle i|u_\alpha(0)\rangle|^2 |\langle u_\beta(0)|j\rangle|^2 \Gamma_{\alpha\beta}. \quad (\text{C9})$$

The obtained $\bar{\Gamma}_{ij}$ allow to define effective transition rates between eigenstates for finite driving amplitudes A . In principle, the rates $\bar{\Gamma}_{kl}$ given by Eq. (C9) can be different than the rates for $A = 0$ given by Eq. (C1). This is illustrated in Fig. 10(b), where we plot the FGR estimates, Eq. (C2), and the rates $\bar{\Gamma}_{kl}$ computed numerically for $A/\omega = 3.8$. In the comparison of $A = 0$ rates with the $A \neq 0$ effective rates we find that in spite of evident differences, the most relevant transition rates, Γ_{12} , that dominates the dynamics for $\xi < \xi_c$, and Γ_{02} , Γ_{23} , that dominate the dynamics for $\xi > \xi_c$, have a similar dependence with ξ . One thus can conclude that the strength of these dominant decay channels is mainly determined by the degree of asymmetry in the qubits-bath couplings, $1 - \xi$, in agreement with the estimates given in Eq. (C2).

Finally, in Fig. 10(c) we compare the effective rates $\bar{\Gamma}_{kl}$ given by Eq. (C9) with the Floquet rates $\Gamma_{\alpha\beta}$, both for $A/\omega = 3.8$, $\epsilon_0/\omega = 3.7$, and $J/\omega = -2.5$. We find that most of the rates labeled by the same indices follow a similar trend with ξ and are in good qualitative agreement. In particular, the rates Γ_{12} , Γ_{02} , and Γ_{23} which dominate the main relaxation processes associated to the O3L mechanisms studied in Sec. III are in good quantitative agreement with their counterparts computed in the Floquet basis, $[\Gamma_{12}]_{\mathcal{F}}$, $[\Gamma_{02}]_{\mathcal{F}}$, and $[\Gamma_{23}]_{\mathcal{F}}$, respectively. The similarity among Γ_{ij} and $\Gamma_{\alpha\beta}$ reflects the fact that, out of resonance, each Floquet state has a principal overlap with the associated eigenstate of the time-independent Hamiltonian for $\Delta_1, \Delta_2 < \omega$ [58].

APPENDIX D: DEPENDENCE ON THE QUBIT-QUBIT COUPLING

A natural question that arises is how the entanglement generation described in Sec. II is modified as the qubit-qubit interaction strength J changes. Figure 11 shows the intensity plot of C_∞ as a function of J/ω and ϵ_0/ω for $\xi = 1$ [Fig. 11(a)] and $\xi = 0.1$ [Fig. 11(b)]. While C_∞ for $\xi = 1$ seems to

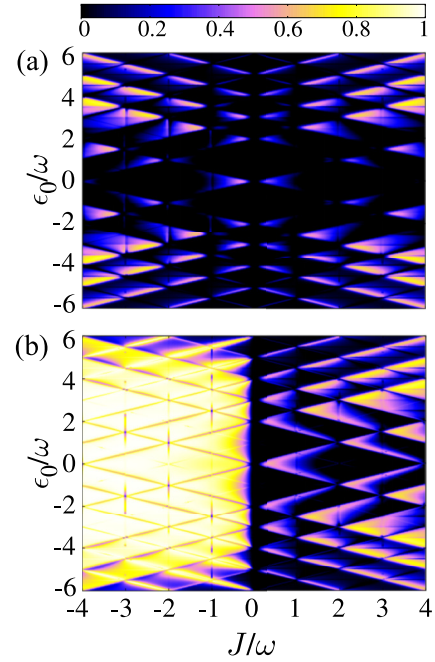


FIG. 11. Intensity plot of C_∞ versus J/ω and ϵ_0/ω for (a) $\xi = 1$ and (b) $\xi = 0.1$. In both cases $A/\omega = 3.8$ while other parameters have the same values as in Fig. 2.

be independent of the sign of J/ω , i.e., $C_\infty(J) \sim C_\infty(-J)$, for $\xi = 0.1$ [Fig. 11(b)], C_∞ exhibits striking differences. Nevertheless, in the two cases we notice the relevance of the resonances among a separable and an entangled state, which correspond to the straight lines defined by $\epsilon_0 \pm |J|/2 = n\omega$ in Fig. 11. The behavior shown in Fig. 11(a) has been extensively discussed in Ref. [15] and we refer the reader to this paper for specific details. To summarize, the triangularlike structure of C_∞ that shows enhanced entanglement at one side of the resonances defined by $\epsilon_0 - |J|/2 \sim m\omega$ (together with its symmetry with the sign of J/ω and antisymmetry with ϵ_0/ω , respectively) is related to the aforementioned N2L mechanism, mediated by the bath and the external driving. Notice that in this case there is not entanglement generated by the O3L mechanism. This is due to the fact that for $\xi = 1$, the relaxation rates that could contribute to populate in the steady state the entangled state $|1\rangle \equiv |e_-\rangle$ for $J < 0$ [$|1\rangle \equiv |e_+\rangle$ for $J > 0$; see Fig. 1(b)] satisfy $\Gamma_{12} \sim 0$ for both signs of J [the analytical estimates for the rates computed in the eigenbasis of H_0 and for $J > 0$ are given by Eq. (3) but with the subindices $1 \leftrightarrow 2$ interchanged, as for $J > 0$ the first and second excited states are $|1\rangle \equiv |e_+\rangle$ and $|2\rangle \equiv |e_-\rangle$, respectively].

Indeed, for $J > 0$ and $\xi = 1$, the relevant relaxation rates tend to populate the $|0\rangle \equiv |s_0\rangle$ separable state, in analogy with the case for $J < 0$ and $\xi = 1$, previously discussed.

Notice that as we have already argued and following the analysis given in Appendix C, the rate computed in the Floquet basis satisfies $[\Gamma_{12}]_{\mathcal{F}} \sim 0$ for $\xi = 1$ and for both signs of J , obeying the same trend as the rate computed in the eigenbasis of H_0 , as Figs. 5 and 12 display.

In the following we discuss the behavior observed in Fig. 11(b) for $\xi = 0.1$. The results for the negative branch $J < 0$ can be understood following the same reasoning as

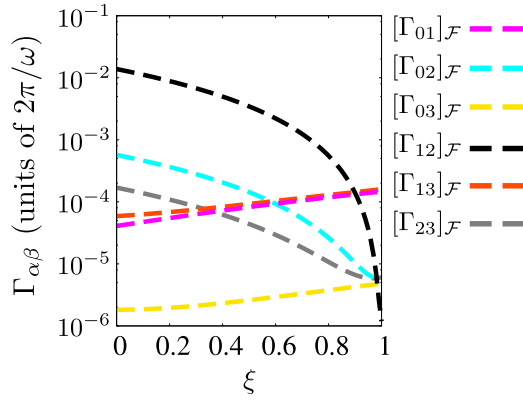


FIG. 12. Transition rates $\Gamma_{\alpha\beta}$, computed in the Floquet basis, as a function of ξ for the off-resonance case $\epsilon_0 = 3.7\omega$. The results correspond to $J/\omega = 2.5$ and $A/\omega = 3.8$. Other parameters are the same as in Fig. 2.

in Sec. II, where we focused on $J/\omega = -2.5$. The value $C_\infty \lesssim 1$ is attained for almost all the explored range of parameter space with largest value $C_\infty \simeq 1$ corresponding to the conditions for the O3L mechanism previously described and with the relaxation rates essentially given by

Eq. (3). As in the present case is $A = 3.8\omega$, the entanglement creation by the O3L mechanism fades out outside the wedge-shaped region delimited by the lines $J/\omega = \pm(\epsilon_0/\omega - 3.8)$, as outside this region is $A < A_c$, and thus the critical amplitude A_c necessary to activate the O3L mechanism is not attained.

A visible feature in Fig. 11(a) is that, superimposed on the quasihomogeneous pattern of $C_\infty \sim 1$, straight lines along which is $C_\infty \sim 0.5$ are clearly observed near the resonance conditions $\epsilon_0 \pm |J|/2 \sim m\omega$, which have been discussed in Sec. IV.

For the positive branch $J > 0$ the O3L mechanism is completely suppressed, and instead there is a triangularlike structure rather similar to Fig. 11(a), i.e., corresponding to entanglement generated by the N2L mechanism. This result can be easily explained as follows. As mentioned before, for $J > 0$, the first and second excited states are switched between each other: $|e_-\rangle \leftrightarrow |e_+\rangle$ ($|1\rangle \leftrightarrow |2\rangle$). As a consequence, for $J > 0$ and $\xi \rightarrow 0$, in addition to $[\Gamma_{12}]_{\mathcal{F}}$, the second relevant relaxation rate is $[\Gamma_{02}]_{\mathcal{F}}$. Thereby, there are now two relaxation mechanisms from the $|2\rangle$ state affecting the dynamics, the $|2\rangle \rightarrow |1\rangle$ transition and the $|2\rangle \rightarrow |0\rangle$ transition. This later mechanism tends to populate the ground state at long times.

- [1] B. Kraus, H. P. Büchler, S. Diehl, A. Kantian, A. Micheli, and P. Zoller, *Phys. Rev. A* **78**, 042307 (2008).
- [2] F. Verstraete, M. M. Wolf, and J. Ignacio Cirac, *Nat. Phys.* **5**, 633 (2009).
- [3] J. T. Barreiro, M. Müller, P. Schindler, D. Nigg, T. Monz, M. Chwalla, M. Hennrich, C. F. Roos, P. Zoller, and R. Blatt, *Nature (London)* **470**, 486 (2011).
- [4] H. Krauter, C. A. Muschik, K. Jensen, W. Wasilewski, J. M. Petersen, J. I. Cirac, and E. S. Polzik, *Phys. Rev. Lett.* **107**, 080503 (2011).
- [5] Y. Lin, J. P. Gaebler, F. Reiter, T. R. Tan, R. Bowler, A. S. Sørensen, D. Leibfried, and D. J. Wineland, *Nature (London)* **504**, 415 (2013).
- [6] F. Reiter, L. Tornberg, G. Johansson, and A. S. Sørensen, *Phys. Rev. A* **88**, 032317 (2013).
- [7] S. Shankar, M. Hatridge, Z. Leghtas, K. M. Sliwa, A. Narla, U. Vool, S. M. Girvin, L. Frunzio, M. Mirrahimi, and M. H. Devoret, *Nature (London)* **504**, 419 (2013).
- [8] Z. Leghtas, U. Vool, S. Shankar, M. Hatridge, S. M. Girvin, M. H. Devoret, and M. Mirrahimi, *Phys. Rev. A* **88**, 023849 (2013).
- [9] D. Kienzler, H.-Y. Lo, B. Keitch, L. de Clercq, F. Leupold, F. Lindenfesler, M. Marinelli, V. Negnevitsky, and J. P. Home, *Science* **347**, 53 (2015).
- [10] M. E. Kimchi-Schwartz, L. Martin, E. Flurin, C. Aron, M. Kulkarni, H. E. Tureci, and I. Siddiqi, *Phys. Rev. Lett.* **116**, 240503 (2016).
- [11] F. Tacchino, A. Auffèves, M. F. Santos, and D. Gerace, *Phys. Rev. Lett.* **120**, 063604 (2018).
- [12] C. M. Quintana, K. D. Petersson, L. W. McFaul, S. J. Srinivasan, A. A. Houck, and J. R. Petta, *Phys. Rev. Lett.* **110**, 173603 (2013).
- [13] P. Campagne-Ibarcq, E. Zolys-Geller, A. Narla, S. Shankar, P. Reinhold, L. Burkhardt, C. Axline, W. Pfaff, L. Frunzio, R. J. Schoelkopf, and M. H. Devoret, *Phys. Rev. Lett.* **120**, 200501 (2018).
- [14] R. Li, D. Yu, S.-L. Su, and J. Qian, *Phys. Rev. A* **101**, 042328 (2020).
- [15] A. L. Gramajo, D. Domínguez, and M. J. Sánchez, *Phys. Rev. A* **98**, 042337 (2018).
- [16] W. D. Oliver, Y. Yu, J. C. Lee, K. K. Berggren, L. S. Levitov, and T. P. Orlando, *Science* **310**, 1653 (2005).
- [17] M. Sillanpää, T. Lehtinen, A. Paila, Y. Makhlin, and P. Hakonen, *Phys. Rev. Lett.* **96**, 187002 (2006).
- [18] D. M. Berns, W. D. Oliver, S. O. Valenzuela, A. V. Shytov, K. K. Berggren, L. S. Levitov, and T. P. Orlando, *Phys. Rev. Lett.* **97**, 150502 (2006).
- [19] M. S. Rudner, A. V. Shytov, L. S. Levitov, D. M. Berns, W. D. Oliver, S. O. Valenzuela, and T. P. Orlando, *Phys. Rev. Lett.* **101**, 190502 (2008).
- [20] A. Izmalkov, S. H. W. van der Ploeg, S. N. Shevchenko, M. Grajcar, E. Il'ichev, U. Hübner, A. N. Omelyanchouk, and H.-G. Meyer, *Phys. Rev. Lett.* **101**, 017003 (2008).
- [21] S. Shevchenko, S. Ashhab, and F. Nori, *Phys. Rep.* **492**, 1 (2010).
- [22] C. M. Wilson, G. Johansson, T. Duty, F. Persson, M. Sandberg, and P. Delsing, *Phys. Rev. B* **81**, 024520 (2010).
- [23] E. Dupont-Ferrier, B. Roche, B. Voisin, X. Jehl, R. Wacquez, M. Vinet, M. Sanquer, and S. De Franceschi, *Phys. Rev. Lett.* **110**, 136802 (2013).
- [24] F. Forster, G. Petersen, S. Manus, P. Hänggi, D. Schuh, W. Wegscheider, S. Kohler, and S. Ludwig, *Phys. Rev. Lett.* **112**, 116803 (2014).

- [25] P. Neillinger, S. N. Shevchenko, J. Bogár, M. Reháč, G. Oelsner, D. S. Karpov, U. Hübner, O. Astafiev, M. Grajcar, and E. Il'ichev, *Phys. Rev. B* **94**, 094519 (2016).
- [26] T. M. Stace, A. C. Doherty, and S. D. Barrett, *Phys. Rev. Lett.* **95**, 106801 (2005).
- [27] T. M. Stace, A. C. Doherty, and D. J. Reilly, *Phys. Rev. Lett.* **111**, 180602 (2013).
- [28] A. Ferrón, D. Domínguez, and M. J. Sánchez, *Phys. Rev. Lett.* **109**, 237005 (2012).
- [29] A. Ferrón, D. Domínguez, and M. J. Sánchez, *Phys. Rev. B* **93**, 064521 (2016).
- [30] A. L. Gramajo, D. Domínguez, and M. J. Sánchez, *Eur. Phys. J. B* **90**, 255 (2017).
- [31] S. Sauer, F. Mintert, C. Gneiting, and A. Buchleitner, *J. Phys. B* **45**, 154011 (2012).
- [32] W.-L. Song, J.-B. You, J. K. Xu, W. L. Yang, and J.-H. An, *Phys. Rev. Appl.* **14**, 054049 (2020).
- [33] J. B. Majer, F. G. Paauw, A. C. J. ter Haar, C. J. P. M. Harmans, and J. E. Mooij, *Phys. Rev. Lett.* **94**, 090501 (2005).
- [34] M. H. S. Amin, *Phys. Rev. B* **71**, 024504 (2005).
- [35] M. Grajcar, A. Izmalkov, S. H. W. van der Ploeg, S. Linzen, T. Plecenik, T. Wagner, U. Hübner, E. Il'ichev, H.-G. Meyer, A. Y. Smirnov, P. J. Love, A. Maassen van den Brink, M. H. S. Amin, S. Uchaikin, and A. M. Zagoskin, *Phys. Rev. Lett.* **96**, 047006 (2006).
- [36] S. H. W. van der Ploeg, A. Izmalkov, A. M. van den Brink, U. Hübner, M. Grajcar, E. Il'ichev, H.-G. Meyer, and A. M. Zagoskin, *Phys. Rev. Lett.* **98**, 057004 (2007).
- [37] Z.-L. Xiang, S. Ashhab, J. Q. You, and F. Nori, *Rev. Mod. Phys.* **85**, 623 (2013).
- [38] F. Yan, S. Gustavsson, A. Kamal, J. Birenbaum, A. P. Sears, D. Hover, T. J. Gudmundsen, D. Rosenberg, G. Samach, S. Weber, J. L. Yoder, T. P. Orlando, J. Clarke, A. J. Kerman, and W. D. Oliver, *Nat. Commun.* **7**, 12964 (2016).
- [39] P. Forn-Díaz, J. García-Ripoll, B. Peropadre, J.-L. Orgiazzi, M. Yurtalan, R. Belyansky, C. M. Wilson, and A. Lupascu, *Nat. Phys.* **13**, 39 (2017).
- [40] Y. Lu, S. Chakram, N. Leung, N. Earnest, R. K. Naik, Z. Huang, P. Groszkowski, E. Kapit, J. Koch, and D. I. Schuster, *Phys. Rev. Lett.* **119**, 150502 (2017).
- [41] S. J. Srinivasan, A. J. Hoffman, J. M. Gambetta, and A. A. Houck, *Phys. Rev. Lett.* **106**, 083601 (2011).
- [42] M. D. Hutchings, J. B. Hertzberg, Y. Liu, N. T. Bronn, G. A. Keefe, M. Brink, J. M. Chow, and B. L. T. Plourde, *Phys. Rev. Appl.* **8**, 044003 (2017).
- [43] A. J. Berkley, H. Xu, R. C. Ramos, M. A. Gubrud, F. W. Strauch, P. R. Johnson, J. R. Anderson, A. J. Dragt, C. J. Lobb, and F. C. Wellstood, *Science* **300**, 1548 (2003).
- [44] A. Izmalkov, M. Grajcar, E. Il'ichev, T. Wagner, H.-G. Meyer, A. Y. Smirnov, M. H. S. Amin, A. Maassen van den Brink, and A. M. Zagoskin, *Phys. Rev. Lett.* **93**, 037003 (2004).
- [45] Y.-x. Liu, L. F. Wei, J. S. Tsai, and F. Nori, *Phys. Rev. Lett.* **96**, 067003 (2006).
- [46] J. Zhang, Y.-x. Liu, C.-W. Li, T.-J. Tarn, and F. Nori, *Phys. Rev. A* **79**, 052308 (2009).
- [47] S. J. Weber, G. O. Samach, D. Hover, S. Gustavsson, D. K. Kim, A. Melville, D. Rosenberg, A. P. Sears, F. Yan, J. L. Yoder, W. D. Oliver, and A. J. Kerman, *Phys. Rev. Appl.* **8**, 014004 (2017).
- [48] F. Yan, P. Krantz, Y. Sung, M. Kjaergaard, D. L. Campbell, T. P. Orlando, S. Gustavsson, and W. D. Oliver, *Phys. Rev. Appl.* **10**, 054062 (2018).
- [49] S. N. Shevchenko, S. H. W. van der Ploeg, M. Grajcar, E. Il'ichev, A. N. Omelyanchouk, and H.-G. Meyer, *Phys. Rev. B* **78**, 174527 (2008).
- [50] E. Il'ichev, S. N. Shevchenko, S. H. W. van der Ploeg, M. Grajcar, E. A. Temchenko, A. N. Omelyanchouk, and H.-G. Meyer, *Phys. Rev. B* **81**, 012506 (2010).
- [51] A. M. Satanin, M. V. Denisenko, S. Ashhab, and F. Nori, *Phys. Rev. B* **85**, 184524 (2012).
- [52] E. A. Temchenko, S. N. Shevchenko, and A. N. Omelyanchouk, *Phys. Rev. B* **83**, 144507 (2011).
- [53] W. D. Oliver and S. O. Valenzuela, *Quantum Inf. Process.* **8**, 261 (2009).
- [54] S. Kohler, T. Dittrich, and P. Hänggi, *Phys. Rev. E* **55**, 300 (1997).
- [55] R. Blattmann, P. Hänggi, and S. Kohler, *Phys. Rev. A* **91**, 042109 (2015).
- [56] S. Kohler, *Phys. Rev. Lett.* **119**, 196802 (2017).
- [57] W. K. Wootters, *Phys. Rev. Lett.* **80**, 2245 (1998).
- [58] J. Hausinger and M. Grifoni, *Phys. Rev. A* **81**, 022117 (2010).
- [59] S. O. Valenzuela, W. D. Oliver, D. M. Berns, K. K. Berggren, L. S. Levitov, and T. P. Orlando, *Science* **314**, 1589 (2006).
- [60] D. L. Campbell, Y.-P. Shim, B. Kannan, R. Winik, D. K. Kim, A. Melville, B. M. Niedzielski, J. L. Yoder, C. Tahan, S. Gustavsson, and W. D. Oliver, *Phys. Rev. X* **10**, 041051 (2020).
- [61] A. L. Gramajo, D. Campbell, B. Kannan, D. K. Kim, A. Melville, B. M. Niedzielski, J. L. Yoder, M. J. Sánchez, D. Domínguez, S. Gustavsson, and W. D. Oliver, *Phys. Rev. Appl.* **14**, 014047 (2020).
- [62] J. H. Shirley, *Phys. Rev.* **138**, B979 (1965).
- [63] M. Grifoni and P. Hänggi, *Phys. Rep.* **304**, 229 (1998).
- [64] A. Ferrón, D. Domínguez, and M. J. Sánchez, *Phys. Rev. B* **82**, 134522 (2010).
- [65] S. Kohler, R. Utermann, P. Hänggi, and T. Dittrich, *Phys. Rev. E* **58**, 7219 (1998).
- [66] H.-P. Breuer, W. Huber, and F. Petruccione, *Phys. Rev. E* **61**, 4883 (2000).
- [67] D. W. Hone, R. Ketzmerick, and W. Kohn, *Phys. Rev. E* **79**, 051129 (2009).
- [68] S. Gasparinetti, P. Solinas, S. Pugnetti, R. Fazio, and J. P. Pekola, *Phys. Rev. Lett.* **110**, 150403 (2013).
- [69] V. Gramich, S. Gasparinetti, P. Solinas, and J. Ankerhold, *Phys. Rev. Lett.* **113**, 027001 (2014).